

Date of publication xxxx 00, 0000, date of current version xxxx 00, 0000.

Digital Object Identifier 10.1109/ACCESS.2019.DOI

User Recognition Based on Human Body Impulse Response: A Feasibility Study

JIN-HO CHUNG¹ (Member, IEEE), TAEWOOK KANG², DOHYUN KWUN¹, JAE-JIN LEE², and SEONG-EUN KIM³ (Member, IEEE)

¹Department of Electrical and Electronic Engineering, Ulsan National Institute of Science and Technology, Ulsan 44919, South Korea

²AI SoC Research Division, Electronics and Telecommunications Research Institute, Daejeon 34129, South Korea

³Department of Electronics and Control Engineering, Hanbat National University, Daejeon 34158, South Korea

Corresponding author: Seong-Eun Kim (e-mail: sekim@hanbat.ac.kr) and Taewook Kang (e-mail: twkang@etri.re.kr)

This work was supported in part by the Electronics and Telecommunications Research Institute (ETRI) funded by the Korean government (No. 19ZB1230), and in part by the National Research Foundation of Korea (NRF) grants funded by the Korea Government (2017R1C1B2012634).

ABSTRACT Human recognition technologies for security systems require high reliability and easy accessibility in the advent of the internet of things (IoT). While several biometric approaches have been studied for user recognition, there are demands for more convenient techniques suitable for the IoT devices. Recently, electrical frequency responses of the human body have been unveiled as one of promising biometric signals, but the pilot studies are inconclusive about the characteristics of human body as a transmission medium for electric signals. This paper provides a multi-domain analysis of human body impulse responses (HBIR) measured at the receiver when customized impulse signals are passed through the human body. We analyzed the impulse responses in the time, frequency, and wavelet domains and extracted representative feature vectors using a proposed accumulated difference metric in each domain. The classification performance was tested using the k -nearest neighbors (KNN) algorithm and the support vector machine (SVM) algorithm on 10-day data acquired from five subjects. The average classification accuracies of the simple classifier KNN for the time, frequency, and wavelet features reached 92.99%, 77.01%, and 94.55%, respectively. In addition, the kernel-based SVM slightly improved the accuracies of three features by 0.58%, 2.34%, and 0.42%, respectively. The result shows potential of the proposed approach for user recognition based on HBIR.

INDEX TERMS Biosignal, human body channel, identification, impulse response, user recognition

I. INTRODUCTION

As the growth of the Internet-of-Things (IoT) technology has accelerated the collection, processing, and dissemination of digital personal information, the social concern about leakage of personal information and the necessity to protect that information are growing, and the extent to which data should be considered as personal information is being investigated [1], [2]. User recognition is being increasingly required to achieve high reliability and easy accessibility to personal information, and it is becoming prevalent in several aspects of life, such as border crossing, access control, administration, social welfare, healthcare, and finance [3]–[5].

Biometric recognition leveraging unique biological characteristics of individuals, including fingerprints [6], [7], face [8], [9], hand geometry [10], iris [11], and voice [12], has been extensively studied given its convenience and accuracy

for personal identification over conventional methods, such as identification cards that can be easily lost or falsified [13], [14]. Still, users are required to properly operate the sensors by conducting specific actions to obtain the desired biometric recognition performance. For example, the user should swipe the finger over a fingerprint sensor at proper speed and alignment. When intrinsic biometric information is mutilated or leaked, it cannot be properly recovered or even cause misidentification [15].

Sensor-based biometric recognition using bio-signals, such as those from electrocardiogram [16], [17], photo-plethysmography [18], and electroencephalogram [19], along with pattern mining provides an alternative to overcome concerns over identity forgery [20], [21]. Pattern mining can be implemented by three main consecutive procedures, namely, data preprocessing with dimensionality reduction,

classification, and clustering and validation based on sensor data acquisition [22]. Its performance can be adjusted by sensor operation and measurements to obtain bio-signals with the desired quality.

In this study, we present a user recognition approach that exploits the human body impulse response (HBIR) to obtain an identification measure, where different delays and amplitudes according to body channel characteristics allow to distinguish individuals. The proposed recognition approach consists of an impulse transmitter (ITx) and an impulse receiver (IRx) based on human body communications (HBC) [23]–[26]. A signal electrode from the ITx applies a narrow pulse signal to the body, and then the IRx electrode receives the HBIR from the body. The previous studies on the body impulse response (HBIR) in [27] and [28] showed the variation of the HBIR for about 70 people measured in a fixed experimental setup, due to the difference of individual intrinsic capacitance affected by different electrical behaviors of cells and fluids in the body [29], which are unique characteristics for respective people. Hence, we were motivated that the HBIR can be adopted as a bio-metric to identify people if the proposed system can detect unique features to distinguish people. Most previous studies in HBC, dealing with the human body channel as a reference for designing a communication system to achieve a maximum data rate or improve the communication stability [30], have presented representative channel models based on statistical analysis using measured data. On the other hand, the aim of this study is to figure out the features leading to channel difference for each person, and to present a method to utilize the factors for distinguishing individuals.

Zensei is an approach to measure the impedance through body tissue characterized by electrical responses between pairs of electrodes for user recognition applications [31], and it has been evaluated over 22-day data from 46 subjects for three different configurations (hand pad, chair, and smartphone). The results showed promising classification accuracy after intense training. An excitation signal generated by a frequency sweep from 1 KHz to 1.5 MHz was employed, and the amplitude and frequency responses of multiple electrode combinations were used for extracting features. Our work focuses on the HBIR across a wide range of frequencies over only a pair of electrodes. In [32], the Fourier transform of the body response to a square wave with width of 100 ns was used to enhance security of PIN entry systems. While presenting the user recognition by experiments conducted using a laboratory wave generator with five subjects over several weeks, the previous studies did not investigate how to extract most identifiable features, such as specific components in the time and frequency domains for classifying individual users.

In our study, we aimed to obtain specific measures that are reliable for distinguishing individuals, such as certain frequency components and time intervals of the HBIR showing unique characteristics for each person based on classification performance evaluated by applying a suitable classification algorithm. In particular, we tried to figure out the factors

to improve the recognition performance in the process of signal processing for classification. Hence, we have applied various technical approaches to obtain unique features in the time, frequency, and wavelet domains with consideration of the implementation feasibility, in terms of signal generation and reception, signal processing, and classification algorithm. The classification performance was evaluated by applying simple classification algorithms such as the *k*-nearest neighbors (KNN) algorithm and the support vector machine (SVM) algorithm [33], [34], for the measured HBIRs from five subjects in terms of the selected measures and by processing the signals in the time, frequency, and wavelet domains. The highest classification accuracy from the five subjects was obtained from the wavelet measure according to sensitivity and specificity analyses. The average classification accuracies for KNN in the time, frequency, and wavelet domains achieved 92.99%, 77.01%, and 94.55%, respectively, while 93.57%, 79.35%, and 94.97% for SVM.

The rest of this paper is organized as follows. Section II presents the principles of electric signal transmission in the human body along with the experimental setup, and detailed experimental procedure and design of the transmission signal to obtain the HBIR. The analysis results for feature extraction using signal processing of the HBIR are reported in section III. Section IV presents performance evaluations applying the KNN and SVM algorithms considering the time, frequency, and wavelet domains. Conclusions are drawn in section VI.

II. SYSTEM MODEL

A. CHANNEL MODEL OF CAPACITIVE COUPLING

There are two methods to apply electric signals to the human body: galvanic coupling and capacitive coupling [35]. The signal and ground electrodes for both the ITx and IRx in galvanic coupling are attached to the body and create signal paths by passing alternating current through the body, regarding the human body as a waveguide [36]. In capacitive coupling, the signal electrode is attached to the body for transmitting and receiving electric signals, while the ground electrode is floating. The signal is generated by forming a current-loop with a signal-electrode attached to the body and a floated ground-electrode coupled with the external-ground, in the both sides of the ITx and IRx. Capacitive coupling can achieve better performance in the frequency range over 60 kHz and signal transmission for longer distances, reaching the arms and legs, than galvanic coupling [37]. Hence, we adopt capacitive coupling for signal transmission to comply with the required frequency band for the HBIR of up to 100 MHz.

Fig. 1 shows the system model to measure the HBIR based on capacitive coupling, where the ITx and IRx are placed on a nonconductive table, and a standing subject keeps the posture by touching ITx and IRx with left- and right-hand fingers, respectively. The signal from the ITx is transmitted to the IRx by changes of the electric field created between the signal and ground electrodes of the IRx. The amplitude of the received signal increases as the ground electrode for both sides of the

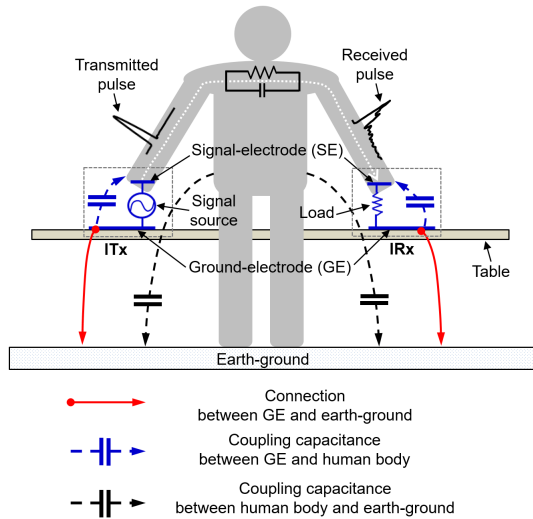


FIGURE 1. System model to measure HBIR based on capacitive coupling.

ITx and IRx are closely coupled with the earth ground and decoupled from the human body [30]. The ground electrodes of the ITx and IRx connected to the earth ground can secure a fixed capacitance to prevent variations from measurement conditions.

The channel model document from the IEEE Standard 802.15.6 wireless body area networks for body surface to body surface over frequency range of 5–50 MHz provides the phase response, amplitude attenuation, and equations to create generalized HBIRs according to the distance between the ITx and IRx and the sizes of ground electrodes [38]. In addition, the human body channel has been interpreted as circuit models using capacitances and resistances to determine the path loss in terms of transmission distance and frequency [29]. Likewise, the signal transmission mechanism on the surface of the human body has been evaluated using theoretical formulations to determine the path loss in terms of transmission distance and frequency [39]. In [27], the channel delay parameters and path loss were obtained from empirical HBIR measurements. HBIR modeling has been proposed using a series of random variables based on measured data [28]. For practical wearable applications, channel modeling for battery-powered devices has been investigated in terms of path loss according to the frequency [40]. The previous study in [41] investigated the channel loss for important measurement issues in the HBC, in terms of ground sharing for a wearable measurement system, dependence on the excitation conditions for capacitive coupling and galvanic coupling, and impedance conditions for the measurement terminations. These works on capacitive coupling have contributed to the development of measurement setups dedicated to the human body channel and presented their unique channel properties by analyzing measured data. With statistical analysis of the measured data, they presented generalized channel models for communication channels in terms of channel path loss according to frequencies, and channel delay parameters, such as coherence

TABLE 1. Human Body Channel Modeling for Communication Systems

Work	Modeling Subject	Measured Data and Analysis
[38]	Path loss and equations for HBIR generation	Path loss with phase response and equations for HBIR for distance and ground-electrode size of the ITx and IRx
[29]	Path loss	Path loss for the human body channel as circuit models
[39]	Theoretical formulations for path loss	Path loss for transmission distance and according to frequency based on Maxwell's equations
[27]	Path loss and delay parameters	Path loss and delay parameters using empirical channel model
[28]	Impulse response modeling	Modeling of the impulse response using a series of random variables based on measured HBIRs
[40]	Path loss	Path loss for battery-powered devices in terms of transmission distance and frequency
[41]	Path loss	Path loss for measurement issues of ground sharing, excitation conditions, and impedance conditions for the measurement terminations

bandwidth, mean delay, and root mean square (RMS) delay spread. Unlike the current studies on the generalization of channel models, our work aimed to identify quantitative features that cause differences in individual HBIRs for applications for user recognition.

B. PROPOSED EXPERIMENTAL SETUP FOR DATA ACQUISITION

We devised a data acquisition platform consisting of customized ITx and IRx. Fig. 2(a) shows an example of the measurement setup and experiment. When a subject touches the electrodes on the ITx and IRx with the left- and right-hand thumbs, respectively, pulse signals from the ITx travel to the IRx through the subject, and then the received HBIR can be measured by an oscilloscope. Fig. 2(b) shows the ITx device with its block diagram and a diagram of the measurement setup. The ITx main components include an Xilinx XC3S200 FPGA [42] to generate a pulse signal of approximately 10 ns, a Texas Instruments TPS61041 DC–DC converter [43] to boost the voltage of the transmitted signal, and a Texas Instruments TLV3501 output buffer [44] to maintain the voltage level by enhancing the current driving capacity when the signal from the ITx is applied to the body. The dimension of the ground electrode, equivalent to that of the device, is $34 \times 52 \text{ mm}^2$. The IRx consists of a signal electrode and a ground electrode of the same dimension as those of the ITx. The signal electrodes of the ITx and IRx contact the corresponding fingers through one-point copper electrodes. The devices are embedded in a transparent non-

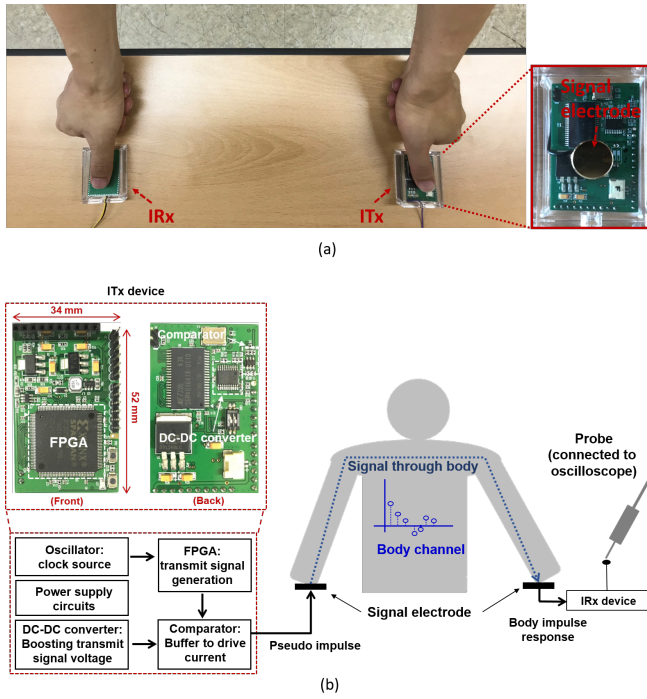


FIGURE 2. (a) An example of measurement experiment. (b) The HBIR measurement with a human subject.

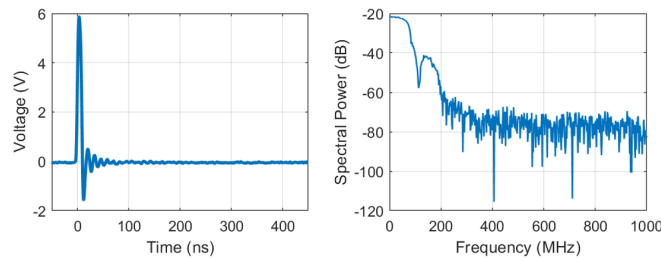


FIGURE 3. Transmitted pseudo impulse signal.

conducting container to avoid unnecessary contacts with the fingers.

Fig. 3 shows a generated pseudo-impulse signal with an approximately 10 ns width and 6 V amplitude, which is repeatedly transmitted for every 1 ms. The impulse signal is a superposition of an infinite number of cosine functions with different frequencies, and its Fourier transform is one over all frequencies. In addition, the narrow pulse signal outperforms every other signal type by a remarkable margin. The sync function of the pulse signal provides a valid flat band reflecting the differences between the magnitude responses of the impulse signal and the corresponding HBIR. The previous study in [32] used a pulse signal with a 100 ns width, while the signals under 10 MHz can be available to be used for the classification. We intended to extend the available signal bandwidth up to 100 MHz using a 10 ns width of the transmitted impulse signal, leading to an increase in the searching region of analysis metrics in the frequency band

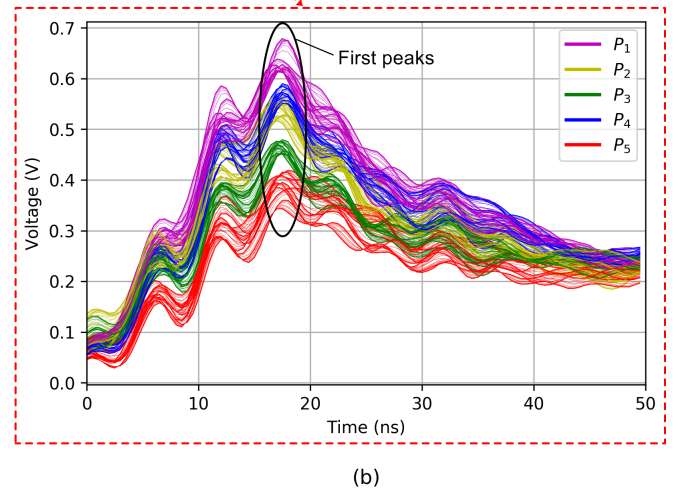
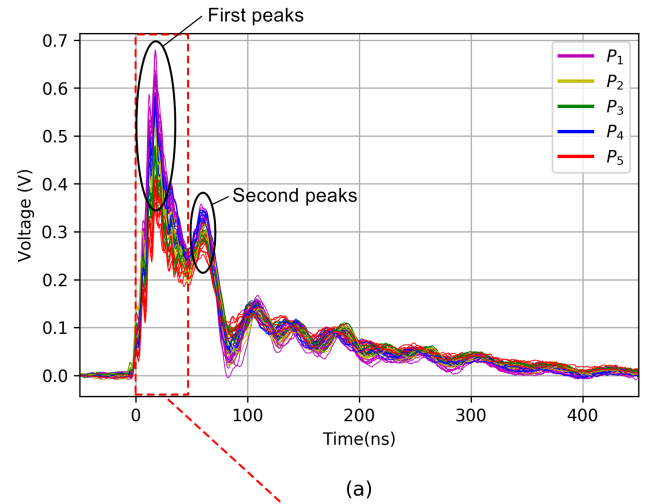


FIGURE 4. HBIR signals from five subjects (100 samples per subject) over (a) the entire time interval -50–450 ns, and (b) the classification period 0–50 ns

such that it is 10 times wider than that of the 100 ns pulse width.

Data were collected from five subjects over approximately 8 weeks considering inter-subject physiological diversity and time-varying physiological changes. Participants were all students from the Hanbat National University in South Korea and voluntarily participated in the study. Each subject was assigned a username for anonymization and asked to provide basic biographical information. The subjects' height was 163–180 cm (mean, 172 cm), their weight was 65–80 kg (mean, 70.6 kg), their age was 20–27 years (mean, 23.7 years), and comprised 2 females and 3 males.

III. FEATURES OF HBIR SIGNALS FOR USER RECOGNITION

To use the measured HBIR signals for user recognition among the five subjects, we analyzed the characteristics in three different domains – time, frequency, and wavelet domains. We arbitrarily indexed the five subjects from P_1 to P_5 .

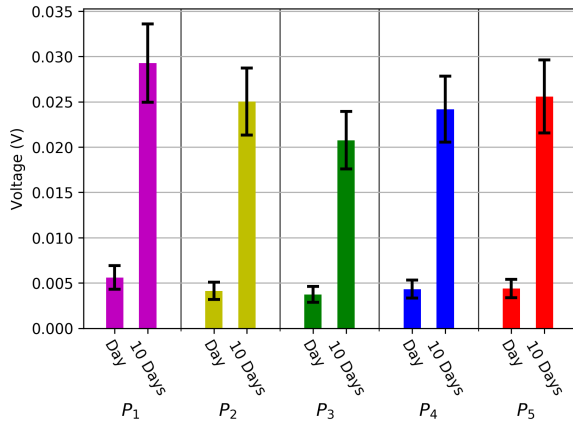


FIGURE 5. Variation of HBIR signals per subject within 1 day and over 10 days

TABLE 2. Variation of first and second peaks in HBIR signals per subject

First Peaks	P_1	P_2	P_3	P_4	P_5
Mean (V)	0.6345	0.5424	0.4677	0.5708	0.3923
Max (V)	0.6794	0.5658	0.4799	0.5939	0.4201
Min (V)	0.6131	0.5166	0.4523	0.5508	0.3427
Second Peaks	P_1	P_2	P_3	P_4	P_5
Mean (V)	0.3337	0.3128	0.2971	0.3377	0.2811
Max (V)	0.3573	0.3327	0.3131	0.3457	0.3060
Min (V)	0.3080	0.2884	0.2824	0.3266	0.2523

A. TIME-DOMAIN ANALYSIS

Fig. 4(a) depicts measured HBIR signals expressed as a voltage for all of the five subjects between -50 and 450 ns, thus including the first and second highest peaks around 18 and 63 ns, respectively. HBIR variations over 10 days and during the same session are depicted in 5. It is observed that 10 consecutive HBIR signals measured on a day show smaller variations in shape and amplitudes per subject than those measured over different days.

Fig. 4(a) depicts measured HBIR signals expressed as a voltage for all of the five subjects between -50 and 450 ns, thus including the first and second highest peaks around 18 and 63 ns, respectively. HBIR variations over 10 days and during the same session are depicted in Fig. 5. It is observed that 10 consecutive HBIR signals measured on a day show smaller variations in shape and amplitudes per subject than those measured over different days. Thus, it may be challenging to recognize a subject from measured HBIR signals. Table 2 lists the means and ranges between the values of maximum and minimum at the first and second highest peaks. The means are distinguishable but the ranges retrieve overlapping values, thus hindering the subject's identification using the HBIR signals.

Each HBIR signal consists of 1,000 data points sampled every 0.5 ns i.e., sampling rate of 2 GHz. Let the HBIR signal of subject P_i be defined as

$$U_{i,xy} = \{U_{i,xy}(n) | 0 \leq n \leq 999\}, \quad (1)$$

for $1 \leq i \leq 5$ and $0 \leq x, y \leq 9$, where i is the subject index, the time index n represents the sample instant between -50 and +449.5 ns with increments of 0.5 ns, the date index x indicates different sessions, and y represents the signal index within one session. To arrange the HBIR signals of subject P_i in terms of first peak values in descending order, the following conditions are assumed:

(I) $U_{i,x0}, U_{i,x1}, \dots, U_{i,x9}$ are measured in the same day;

(II) $\max_n \{U_{i,x0}(n)\} \geq \max_n \{U_{i,x1}(n)\} \geq \dots \geq \max_n \{U_{i,x9}(n)\}$;

(III) $\max_n \{U_{i,00}(n)\} \geq \max_n \{U_{i,10}(n)\} \geq \dots \geq \max_n \{U_{i,90}(n)\}$

for any $1 \leq i \leq 5$ and $0 \leq x \leq 9$. Condition (I) groups the HBIR signals from a subject within a day. Condition (II) indicates that the grouped HBIR signals are arranged in descending order according to the highest peaks. By Condition (III), the grouped HBIR signals among different dates are also ordered according to the magnitudes of highest peaks.

After arranging the HBIR signals, we determine a 100-data point interval to maximize the group distance of HBIR signals among different subjects for classification. Hence, the most distinguishable interval can be chosen by avoiding the ambiguity by overlapping intervals. As the interval between -50 and 0 ns does not contain representative information, it is excluded from our analysis. At instant k with $100 \leq k \leq 999$, we define

$$D_\sigma[k] = (U_{\sigma(1),99}(k) - U_{\sigma(2),00}(k)) + (U_{\sigma(2),99}(k) - U_{\sigma(3),00}(k)) + (U_{\sigma(3),99}(k) - U_{\sigma(4),00}(k)) + (U_{\sigma(4),99}(k) - U_{\sigma(5),00}(k)),$$

where S_5 is the set of all permutations on $\{1, 2, 3, 4, 5\}$. The difference measure $D_\sigma[k]$ is sum of differences between the minimum of a subject and the maximum of another one subject at that time, in which the five subjects are sorted according to permutation σ . If we accumulate the difference through 100 data points for a fixed σ , it can show how the subjects are separated from each other on that interval. For a given n , we call $\max_{\sigma \in S_5} \sum_{k=n}^{n+99} D_\sigma[k]$ the accumulated difference. Fig. 6 shows the accumulated difference for $100 \leq n \leq 899$. Larger values of the accumulated difference at the corresponding time interval indicate higher distinguishability among subjects, whereas small values indicate overlapping HBIR signals among subjects in the corresponding intervals. Thus, this measure can be used to assess how subjects are distinguishable to each other over the time interval. The initial time index of a refined interval can be defined as

$$n_{\max} = \arg \max_{100 \leq n \leq 899} \left\{ \max_{\sigma \in S_5} \sum_{k=n}^{n+99} D_\sigma[k] \right\}. \quad (2)$$

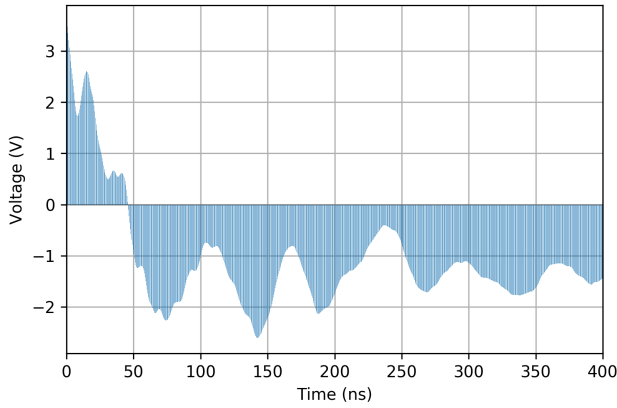


FIGURE 6. Accumulated differences in 0–400 ns

Given that n_{\max} is the initial point of the interval that satisfies the maximum accumulated difference, the interval $[n_{\max}, n_{\max} + 99]$ is the classification interval for HBIR signals in the time domain. The classification interval can be considered from 0 to 50 ns, where the maximum value of the accumulated difference is achieved at $n = 100$ corresponding to 0 ns with $\sigma = (1\ 4\ 2\ 3\ 5)$. The HBIR signals in the classification interval are depicted in Fig. 4(b).

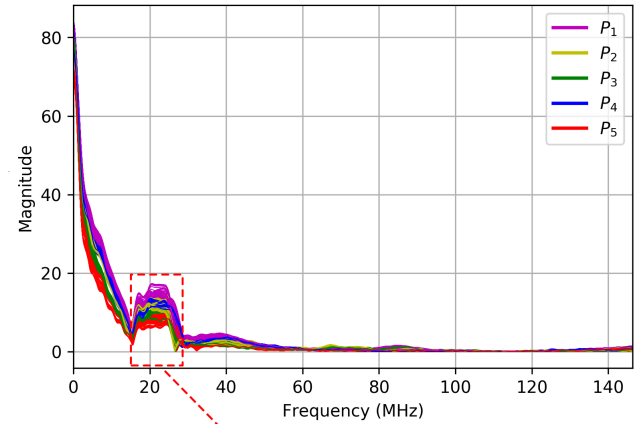
B. FREQUENCY-DOMAIN ANALYSIS

The acquired HBIR signals have 1,000 data points sampled at 2 GHz, and hence the 1,000-point fast Fourier transform (FFT) gives a resolution of 2 MHz. Considering the transmitted pulse width of 10 ns, we can consider that the representative signal power is concentrated below 100 MHz. Then, we have only 50 points for that frequency band, which is insufficient for analysis. The frequency resolution is determined by the time length of the original signal, T , as $\Delta R = 1/T$, but we can improve the FFT resolution by applying zero-padding to the HBIR signal [45]. The total length of the HBIR signal increases to 16,384 points, and this signal is transformed into the frequency domain by the FFT. According to our choice of FFT length, the bandwidth of our 100-point classification interval in the frequency domain is approximately 12.2 MHz. Fig. 7(a) shows the magnitude response of the HBIR signal obtained from the 16384-point FFT. The frequency domain data is plotted with linear scale in accordance with the time-domain plot.

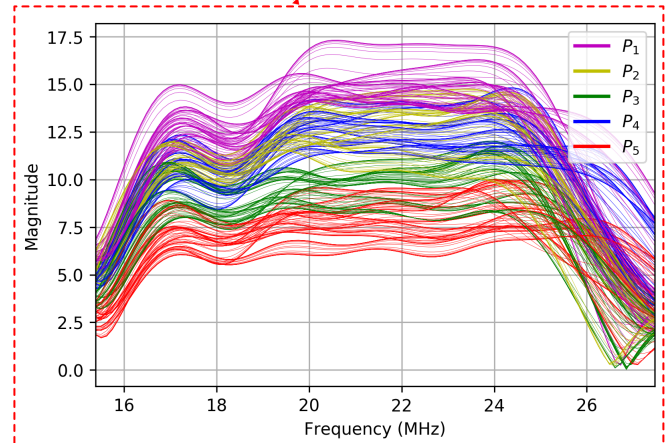
As defined in (2), the magnitude response of each HBIR signal can be represented as

$$W_{i,xy} = \{W_{i,xy}(m) | 0 \leq m \leq 16383\} \quad (3)$$

where $W_{i,xy}$ corresponds to the magnitude response of $U_{i,xy}$ for $1 \leq i \leq 5$ and $0 \leq x, y \leq 9$. Similar to the time domain, the initial index of the target interval used for classification



(a)



(b)

FIGURE 7. Magnitude response of HBIR signals over (a) 0–140 MHz and (b) the classification interval 15.5–27.7 MHz in linear scale

can be determined by

$$m_{\max} = \arg \max_{0 \leq m \leq 16284} \left\{ \max_{\sigma \in S_5} \sum_{l=m}^{m+99} E_{\sigma}[l] \right\} \quad (4)$$

where

$$\begin{aligned} E_{\sigma}[l] = & (W_{\sigma(1),99}(l) - W_{\sigma(2),00}(l)) \\ & + (W_{\sigma(2),99}(l) - W_{\sigma(3),00}(l)) \\ & + (W_{\sigma(3),99}(l) - W_{\sigma(4),00}(l)) \\ & + (W_{\sigma(4),99}(l) - W_{\sigma(5),00}(l)). \end{aligned}$$

The optimal m_{\max} retrieving the maximum accumulated difference is 127 and interval $[m_{\max}, m_{\max} + 99] = [127, 226]$ is selected for classification. Its corresponding frequency band is between 15.5 and 27.7 MHz as shown in Fig. 7(b).

C. WAVELET ANALYSIS

In both the time and frequency domains, we found that the HBIR signals from different subjects overlap across several points as shown in Figs. 4 and 7. To recognize the subjects,

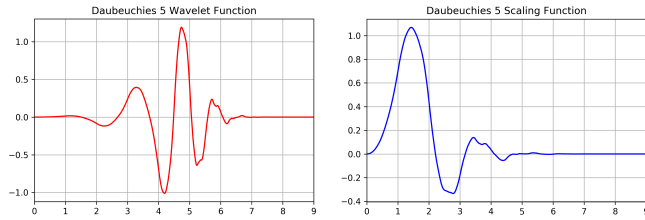


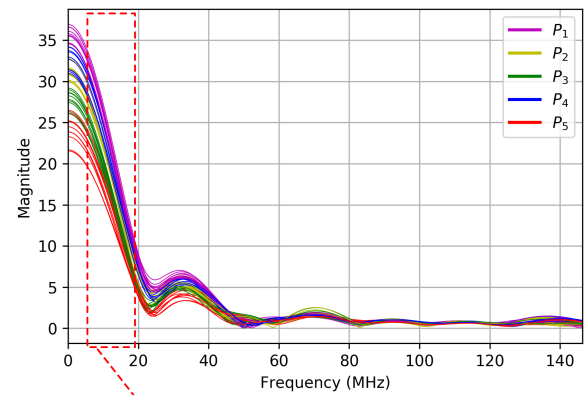
FIGURE 8. Wavelet and scaling functions Daubechies 5 for DWT

we selected 100-point intervals with the maximum accumulated difference. Because the FFT is applied through the entire time interval, it cannot sufficiently reflect the time-varying features of the HBIR signals. In this section, a time-frequency analysis based on the wavelet transform is considered. Time-varying spectrum is subdivided into overlapping windows and estimated locally at each window using Fourier or wavelet based methods. The wavelet transform gives time-frequency localization by decomposition with multi-resolution [46], [47]. If wavelets are sampled at discrete times in the wavelet transform, it is called a discrete wavelet transform (DWT). It allows us to analyze time-varying properties of sampled signals. The DWT has different representations depending on the type of mother wavelet employed. Daubechies wavelets [48] have been commonly used in classification of one-dimensional signals such as those from electroencephalography and electrocardiography [49], [50]. Hence, we adopted the Daubechies 5 as wavelet function, along with its scaling function. Fig. 8 shows the wavelet and scaling functions of Daubechies 5.

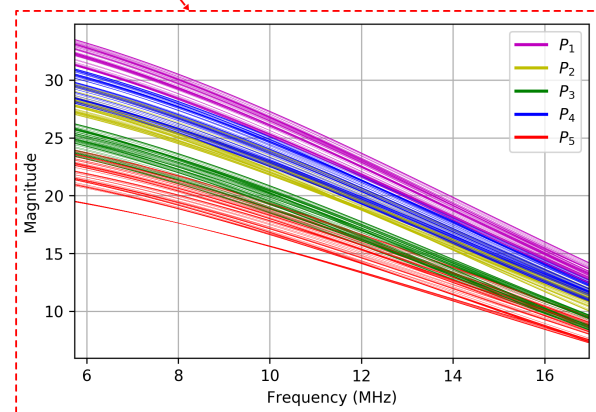
In our time-domain analysis, we found that time signals over 0-50 ns could be significant features to maximize the accumulative distance. We want to extract high-level features from the time segment by using wavelet decomposition based on DWT, ultimately, to improve the classification accuracy. The DWT creates approximated and detailed coefficients in terms of decomposition levels. At each level, the coefficients provide decomposition of the signal in lower- and upper-half frequencies, respectively. For an HBIR signal $U_{i,xy}$, the DWT present decomposition of different levels as

$$\begin{aligned} U_{i,xy} &= a_{i,xy}^{(1)} + d_{i,xy}^{(1)} \\ &= a_{i,xy}^{(2)} + d_{i,xy}^{(2)} + d_{i,xy}^{(1)} \\ &= \dots \\ &= a_{i,xy}^{(h)} + \sum_{l=1}^h d_{i,xy}^{(l)} \end{aligned}$$

where $a_{i,xy}^{(l)} = \{a_{i,xy}^{(l)}(n) | 0 \leq n \leq 999\}$ is the decomposition with the approximate coefficients, and $d_{i,xy}^{(l)} = \{d_{i,xy}^{(l)}(n) | 0 \leq n \leq 999\}$ is the decomposition with the detailed coefficients at level l , respectively. The covered frequency ranges are $[0, 2 \cdot 10^9/2^l]$ MHz for decomposition with the approximate coefficients, and $[2 \cdot 10^9/2^l, 2 \cdot 10^9/2^{l-1}]$ MHz for decomposition with the detailed coefficients of level l , respectively.



(a)



(b)

FIGURE 9. FFT of the time-domain segment of 0-50 ns over (a) 0-140 MHz and (b) 6-16 MHz in linear scale

To select the best decomposition in DWT for classification, we observed the FFT of the classification interval for the time-domain segment of 0-50 ns (Fig. 9). In the frequency spectrum of the segment, 7-16 MHz is the most distinguishable band, which include the range 7.8-15.6 MHz of the decomposed signal with detailed coefficients of level 8. Hence, classification with the decomposition $d_{i,xy}^{(8)}$ is expected to outperform classification with the time-domain segment of 0-50 ns.

IV. CLASSIFICATION RESULTS

A. PROCESS OF CLASSIFICATION

For classification of the HBIR signals, we adopted two supervised machine learning algorithms - the KNN algorithm [33] and the SVM algorithm [34]. The KNN algorithm can be employed for classification and regression with low complexity, and is easy to implement. In the algorithm, the k nearest neighborhoods of a target sample are determined according to a metric, such as the Euclidean distance. Then, a decision is made upon the group with the highest number of neighbors. In the SVM algorithm, a support vector machine create a hyperplane for classification in a high- or infinite-dimensional space. When it is too hard to separate a given

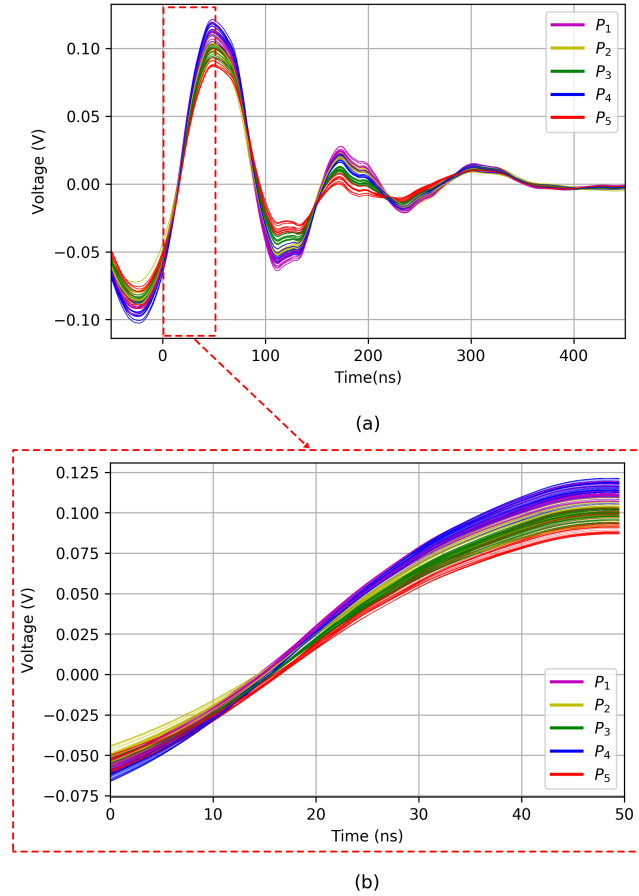


FIGURE 10. Decomposed signals with detailed coefficients at level 8 in Daubechies 5 DWT over (a) the entire time interval and (b) the classification interval

data set with linear classification, a kernel trick is applied to the data set. The radial basis function (RBF) kernel [51] is most commonly used, and it shows good performance in ordinary cases.

For time-domain HBIR signals, let $\hat{U}_{i,xy}$ be a segmentation of $U_{i,xy}$ that consists of 100 points specified by the classification interval calculated in Section III.A, which is given by

$$\hat{U}_{i,xy} = \{U_{i,xy}(n) | n_{\max} \leq n \leq n_{\max} + 99\}. \quad (5)$$

Then, the total dataset of segmentation for each subject, $\hat{U}_i = \{\hat{U}_{i,xy} | 0 \leq x, y \leq 9\}$, can be partitioned into 10 groups by date and represented by

$$\hat{U}_i = \bigcup_{x=0}^9 \hat{U}_{i,x}, \quad (6)$$

where $\hat{U}_{i,x} = \{\hat{U}_{i,x0}, \hat{U}_{i,x1}, \dots, \hat{U}_{i,x9}\}$ is a set of segmented HBIR signals successively measured within a day. By using 10 data groups, we evaluated the classification performance with 10-fold cross-validation which is equivalent to leave-one-out cross-validation in our setup. The goal of cross-validation is to test the performance to predict new data that were not used in training, and thus mitigate overfitting. We

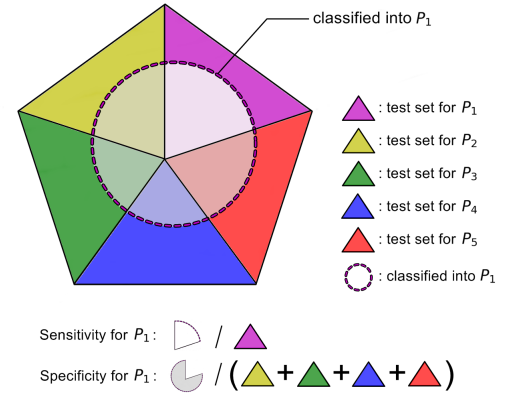


FIGURE 11. The example of sensitivity and specificity for identification of P_1

have 10 sets and one by one, a set is randomly selected as test set. Then, the other 9 sets are used for training until all possible combinations are evaluated. The classification results show that subjects can be identified using training sets acquired at different dates.

Let σ_i be a permutation on $\{1, 2, \dots, 10\}$ for subject P_i . At the j -th test of the 10-fold validation, the HBIR signals with date index $\sigma_i(j)$ are selected as the test set:

$$\text{Test set} = \bigcup_{i=1}^5 \hat{U}_{i,\sigma_i(j)};$$

$$\text{Training set} = \bigcup_{i=1}^5 (\hat{U}_i \setminus \hat{U}_{i,\sigma_i(j)}),$$

where $A \setminus B$ denotes the set difference between two sets A and B , that is, the resulting set consists of the elements of A which are not in B . Then, the KNN algorithm is tested on the training and test sets. The best choice of k depends on the data and we set $k = 17$ by a cross-validation check. For SVM, we selected $C = 1$ and $\gamma = 10^{-2}$ as the parameters of the RBFs. At the j -th test, if a sample $\hat{U}_{i,\sigma_i(j)y}$ in the test set is correctly classified to subject P_i , it can be regarded as a correct detection or a true positive. We tested the 10-fold validation for 50 different combinations of $\{\sigma_1, \sigma_2, \dots, \sigma_5\}$.

B. RESULTS OF USER RECOGNITION

The sensitivity, or true positive rate, is defined as the number of true positives divided by the number of actually positive samples (Fig. 11). Table 3 lists the classification results in terms of sensitivity. In the time and wavelet domains, the sensitivity is above 90%, except for P_2 , while sensitivity below 70% is obtained for P_2 and P_4 in the frequency domain. The confidence interval of sensitivity for KNN is depicted in Fig. 12(a).

The specificity, or true negative rate, measures the proportion of false positives over actually negative samples (Fig. 11). In almost all the cases, the average specificity for KNN is above 95% as shown in Table 3. Hence, the probability of a false positive is very low. Moreover, the variance of the

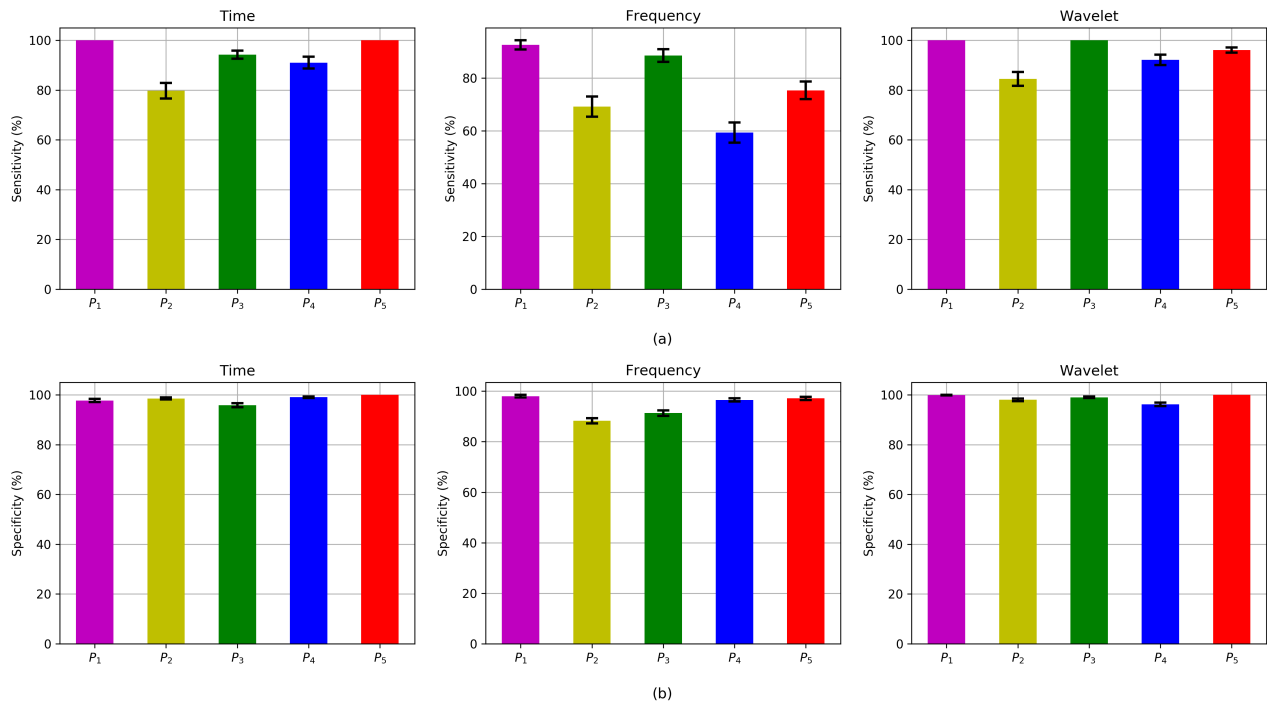


FIGURE 12. 95% confidence interval of (a) sensitivity and (b) specificity of classification by KNN (%)

TABLE 3. Average sensitivity and specificity of classification using KNN in different domains (%)

Time	P ₁	P ₂	P ₃	P ₄	P ₅
Sensitivity	100	79.7	94.2	91.0	100
Specificity	97.8	98.6	95.8	99.1	100
Frequency	P ₁	P ₂	P ₃	P ₄	P ₅
Sensitivity	92.6	69.2	88.6	59.3	75.3
Specificity	98.0	88.1	91.3	96.5	97.1
Wavelet	P ₁	P ₂	P ₃	P ₄	P ₅
Sensitivity	100	84.5	100	92.1	96.1
Specificity	99.9	98.0	99.0	96.2	100

TABLE 4. Classification accuracy using KNN and SVM (%)

KNN	Time	Frequency	Wavelet
Average	92.99	77.01	94.55
Maximum	96.2	81.4	95.0
Minimum	92.0	75.2	94.2
Variance	1.37×10^{-4}	2.36×10^{-4}	5.25×10^{-6}
SVM	Time	Frequency	Wavelet
Average	93.57	79.35	94.97
Maximum	96.4	83.8	95.6
Minimum	89.8	78.0	93.6
Variance	1.35×10^{-4}	1.34×10^{-4}	1.56×10^{-5}

specificity is much smaller than that of sensitivity, as shown in Fig. 12(b).

The classification accuracy can be defined as the number of correct detection over the total number of test samples. As listed in Table 4, the average accuracy of our test is above 90% in the time and wavelet domains, and below 80% in the frequency domain. Moreover, the results in the wavelet domain show the smallest variation for different choices of $\{\sigma_1, \dots, \sigma_5\}$. Classification in the wavelet domain shows the best performance for both KNN and SVM, as in Table 4. It can be deduced that our selection of decomposition level by DWT in subsection III.C correctly extract distinguishable frequency components from the time-domain segment of 0–50 ns.

V. CONCLUSION

The reliability of a user recognition method employing a bio-metric is evaluated, which is based on HBIR differences caused by distinctive features of individual human body

channels. The HBIR signals of the human body were acquired for five subjects using customized impulse signals. The proposed signal processing on the measured data allowed to derive effective measures for distinguishing subjects in the time, frequency, and wavelet domains. The highest average classification accuracy of 94.55% for KNN (94.97% for SVM) was obtained in the wavelet domain, in which the classification range was extracted from time-frequency analysis of HBIR signals.

In this study, we investigated the feasibility of using HBIR for user recognition in a small group, such as a household, but five subjects are not enough to fully cover physiological variations of HBIR. Indeed, it is very important to analyze how many users can be recognized by HBIR, which will be investigated in further work. Moreover, due to limitation of the sampling rate provided by the oscilloscope, the activities at low frequencies below 1 MHz was not analyzed. A higher sampling rate will enable HBIR to capture even more be-

havioral and physiological features. As future work, we plan to investigate how low-frequency features can help improve accuracy. Furthermore, we will develop a customized sensing hardware to measure specific HBIR signals employing distinctive features.

ACKNOWLEDGMENT

The authors would like to thank Ms. E.-J. Kang at Hanbat National University for collecting human body impulse response data.

REFERENCES

- [1] J. Gubbi, R. Buyya, S. Marusic, and M. Palaniswami, "Internet of Things (IoT): A vision, architectural elements, and future directions," *Future Generation Computer Systems*, vol. 29, no. 7, pp. 1645–1660, Sep. 2013.
- [2] S. Pearson and A. Benameur, "Privacy, security and trust issues arising from cloud computing," in *Proc. IEEE 2nd Int. Conf. Cloud Comput. Technol. Sci. (CloudCom)*, Nov. 2010, pp. 693–702.
- [3] D. He and S. Zeadally, "Authentication protocol for an ambient assisted living system," *IEEE Commun. Mag.*, vol. 35, no. 1, pp. 71–77, Jan. 2015.
- [4] A. Hiltgen, T. Kramp, and T. Weigold, "Secure Internet banking authentication," *IEEE Security Privacy*, vol. 4, no. 2, pp. 21–29, Mar. 2006.
- [5] Y. Chen, W. Xu, L. Peng, and H. Zhang, "Light-weight and privacy-preserving authentication protocol for mobile payments in the context of IoT," *IEEE Access*, vol. 7, pp. 15210–15221, Jan. 2019.
- [6] D. Valdes-Ramirez et al., "A review of fingerprint feature representations and their applications for latent fingerprint identification: trends and evaluation," *IEEE Access*, vol. 7, pp. 15210–15221, Jan. 2019.
- [7] R. Cappelli, D. Maio, D. Maltoni, J. L. Wayman, and A. K. Jain, "Performance evaluation of fingerprint verification systems," *IEEE Trans. Pattern Anal. Mach. Intell.*, vol. 28, no. 1, pp. 3–18, Jan. 2006.
- [8] T. Ahonen, A. Hadid, and M. Pietikäinen, "Face description with local binary patterns: Application to face recognition," *IEEE Trans. Pattern Anal. Mach. Intell.*, vol. 28, no. 12, pp. 2037–2041, Dec. 2006.
- [9] C. Ding, J. Choi, D. Tao, and L. S. Davis, "Multi-directional multi-level dual-cross patterns for robust face recognition," *IEEE Trans. Pattern Anal. Mach. Intell.*, vol. 38, no. 3, pp. 518–531, Mar. 2016.
- [10] G. Zheng, C. J. Wang, and T. E. Boulton, "Application of projective invariants in hand geometry biometrics," *IEEE Trans. Inf. Forensics Security*, vol. 2, no. 4, pp. 758–768, Dec. 2007.
- [11] L. Ma, T. Tan, Y. Wang, and D. Zhang, "Personal identification based on iris texture analysis," *IEEE Trans. Pattern Anal. Mach. Intell.*, vol. 25, no. 12, pp. 1519–1533, Dec. 2003.
- [12] J. H. L. Hansen and T. Hasan, "Speaker recognition by machines and humans: A tutorial review," *IEEE Signal Process. Mag.*, vol. 32, no. 6, pp. 74–99, Nov. 2015.
- [13] A. K. Jain, A. Ross, and S. Pankanti, "Biometrics: A tool for information security," *IEEE Trans. Inf. Forens. Security*, vol. 1, no. 2, pp. 125–143, Jun. 2006.
- [14] Z. Rui and Z. Yan, "A survey on Biometric Authentication: toward secure and privacy-preserving identification," *IEEE Access*, vol. 7, pp. 5994–6009, Dec. 2018.
- [15] S. Prabhakar, S. Pankanti, and A. K. Jain, "Biometric recognition: Security and privacy concerns," *IEEE Security Privacy*, vol. 1, no. 2, pp. 33–42, Mar./Apr. 2003.
- [16] H. Ko et al., "ECG-based advanced personal identification study with adjusted (Qi * Si)," *IEEE Access*, vol. 7, pp. 40078–40084, Mar. 2019.
- [17] N. Karimian, Z. Guo, M. Tehranipoor, and D. Forte, "Highly reliable key generation from electrocardiogram (ECG)," *IEEE Trans. Biomed. Eng.*, vol. 64, no. 6, pp. 1400–1411, Jun. 2017.
- [18] U. Yadav, S.N.Abbas, and D. Hatzinakos, "Evaluation of PPG biometrics for authentication in different states" *The 11th IAPR International Conference on Biometrics (ICB)*, Goldcoast, Australia, Feb. 2018.
- [19] Y. Di et al., "Robustness analysis of identification using resting-state EEG signals," *IEEE Access*, vol. 7, pp. 42113–42122, Mar. 2019.
- [20] Y. Kwon and J. Kim, "Analysis of bio-signal sensor requirements for personal authentication," in *Proc. 40th Annu. Int. Conf. IEEE EMBC*, Honolulu, HI, Jul. 2018, pp. 1–1.
- [21] J. Chaki, N. Dey, F. Shi, and R. S. Sherratt, "Pattern mining approaches used in sensor-based biometric recognition: A review," *IEEE Sensors J.*, vol. 19, no. 10, pp. 3569–3580, May. 2009.
- [22] E. P. Kukula, M. J. Sutton, and S. J. Elliott, "The human-biometric-sensor interaction evaluation method: Biometric performance and usability measurements," *IEEE Trans. Instrum. Meas.*, vol. 59, no. 4, pp. 784–791, Apr. 2010.
- [23] T. G. Zimmerman, "Applying electric field sensing to human-computer-interfaces," in *Proc. CHI*, 1995, pp. 280–287.
- [24] T. G. Zimmerman, "Personal area networks: Near-field intrabody communication," *IBM Syst. J.*, vol. 35, no. 3–4, pp. 609–617, 1996.
- [25] M. S. Wegmüller, A. Kuhn, J. Froehlich, M. Oberle, N. Felber, N. Kuster, and W. Fichtner, "An attempt to model the human body as a communication channel," *IEEE Trans. Biomed. Eng.*, vol. 54, no. 10, pp. 1851–1857, Oct. 2007.
- [26] Abdelhay Ali et al., "Efficient Autoencoder-Based Human Body Communication Transceiver for WBAN," *IEEE Access*, vol. 7, pp. 117196–117205, Aug. 2019.
- [27] J. H. Hwang, T. W. Kang, S. O. Park, and Y. T. Kim, "Empirical channel model for human body communication," *IEEE Antennas Wireless Propag. Lett.*, vol. 14, pp. 694–697, 2015.
- [28] J. H. Hwang, T. W. Kang, Y. T. Kim, and S. O. Park, "Measurement of transmission properties of HBC channel and its impulse response model," *IEEE Trans. Instrum. Meas.*, vol. 65, no. 1, pp. 177–188, Jan. 2016.
- [29] Pereira, M.D., Alvarez-Botero, G.A., and de Sousa, F.R., "Characterization and modeling of the capacitive HBC channel," *IEEE Trans. Instrum. Meas.*, vol. 64, no. 10, pp. 2626–2635, Oct. 2015.
- [30] T. Kang, K. Oh, J. Hwang, S. Kim, H. Park, and J. Lee, "Measurement and analysis of electric signal transmission using human body as medium for WBAN applications," *IEEE Trans. Instrum. Meas.*, vol. 67, no. 3, pp. 527–537, Mar. 2018.
- [31] Munechiko Sato, et. al. "Zensei: embedded, multi-electrode bioimpedance sensing for implicit, ubiquitous user recognition," *ACM CHI'17*, May. 2017.
- [32] K. B. Rasmussen, M. Roeschlin, I. Martinovic, and G. Tsudik, "Authentication using pulse-Response biometrics," *Communications of the ACM*, vol. 60, no. 2, pp. 108–115, Feb. 2017.
- [33] N. S. Altman, N. S. "An introduction to kernel and nearest-neighbor nonparametric regression," *The American Statistician*, vol. 46, no. 3, pp. 175–185, Jan. 1992.
- [34] C. Cortes and V. Vapnik, "Support-vector networks," *Machine Learning*, vol. 20, no. 3, pp. 273–297, Sept. 1995.
- [35] M. Seyed, B. Kibret, D.T.H. Lai, and M. Faulkner, "A survey on intra-body communications for body area network applications," *IEEE Trans. Biomed. Eng.*, vol. 60, no. 8, pp. 2067–2079, Aug. 2013.
- [36] W. J. Tomlinson, S. Banou, Ch. Yu, M. Stojanovic, and K. R. Chowdhury "Comprehensive Survey of Galvanic Coupling and Alternative Intra-Body Communication Technologies," *IEEE Commun. Surveys Tuts.*, vol. 21, no. 2, pp. 1145–1164, 2nd Quart. 2019.
- [37] M. A. Callejon, D. Naranjo-Hernandez, J. Reina-Tosina, and L. M. Roa, "A comprehensive study into intrabody communication measurements," *IEEE Trans. Instrum. Meas.*, vol. 62, no. 9, pp. 2446–2455, Sep. 2013.
- [38] *Channel Model for Body Area Network (BAN)*, IEEE P802.15-08-0780-12-0006, Nov. 2010.
- [39] J. Bae, K. Song, H. Lee, H. Cho, and H. J. Yoo, "The signal transmission mechanism on the surface of human body for body channel communication," *IEEE Trans. Microw. Theory Tech.*, vol. 60, no. 3, pp. 582–593, Mar. 2012.
- [40] J. Park, H. Garudadri and P. P. Mercier, "Channel modeling of miniaturized battery-powered capacitive human body communication systems," *IEEE Trans. Biomed. Eng.*, vol. 64, no. 2, pp. 452–462, Feb. 2017.
- [41] S. Maity et al., "BioPhysical modeling, characterization and optimization of electroquasistatic human body communication," *IEEE Trans. Biomed. Eng.*, vol. 60, no. 6, pp. 1791–1802, June. 2019.
- [42] Xilinx. *Spartan-3 FPGA Family Data Sheet*. Accessed: Jun. 27, 2013. [Online]. Available: <https://www.xilinx.com/support/documentation/datasheets/ds099.pdf>
- [43] Texas Instrument. *TPS6104x Low-Power DC-DC Boost Converter in SOT-23 and WSON Packages*. Accessed: Oct. 2018. [Online]. Available: <http://www.ti.com/lit/ds/symlink/tps61040.pdf>
- [44] Texas Instrument. *TLV350x 4.5-ns, Rail-to-Rail, High-Speed Comparator in Microsize Packages*. Accessed: Apr. 2016. [Online]. Available: <http://www.ti.com/lit/ds/symlink/tlv3502.pdf>

- [45] Steven S. Smith, *The Scientist and Engineer's Guide to Digital Signal Processing*. 2nd Ed., California Technical Publishing, 1999.
- [46] S. G. Mallat, "A theory for multiresolution signal decomposition: the wavelet representation," *IEEE Trans. Pattern Anal. Mach. Intell.*, vol. 11, no. 7, pp. 674–693, Jul. 1989.
- [47] Charles K. Chui, *An Introduction to Wavelets*. San Diego: Academic Press, 1992.
- [48] I. Daubechies, "Orthonormal bases of compactly supported wavelets," *Communications on Pure and Applied Mathematics*, vol. 41, no. 7, pp. 909–996, 1988.
- [49] N. Hazarika, J. Z. Chen, A. C. Tsoi, and A. Sergejew, "Classification of EEG signals using the wavelet transform," *Signal Processing*, vol. 59, pp. 61–72, 1997.
- [50] M. A. Mohamed and M. A. Deriche, "An approach for ECG feature extraction using Daubechies 4 wavelet," *International Journal of Computer Applications*, vol. 96, no. 12, pp. 36–41, Jun. 2014.
- [51] D. S. Broomhead and D. Lowe, "Multivariable functional interpolation and adaptive networks," *Complex Systems*, vol. 2, no. 3, pp. 321–355. 1988.